J. Fluid Mech. (1974), *vol.* 65, *part* 4, *pp.* 689–710
Printed in Great Britain

Dynamics of establishment of selective withdrawal of a stratified fluid from a line sink. Part 2. Experiment

By TIMOTHY W. KAO, HSIEN-PING PAO AND SHUANG N. WEI

The Department of Aerospace and Atmospheric Sciences, The Catholic University of America, Washington, D.C. 20017

(Received 30 August 1973 and in revised form 4 March 1974)

Experiments were conducted to examine the development and establishment of the withdrawal current in the selective withdrawal of a stratified fluid from a line sink. The experiments were performed in a Plexiglas channel 30·5 ft long 14 in. wide, and filled with a linearly stratified salt solution to a depth of 18 in. The line sink was located at mid-depth. The flow was symmetric about the mid-depth. Velocity measurements and flow visualization were obtained by neutrally buoyant liquid droplets and vertical dye lines. Density measurements were made by a salinity probe. The development of the upstream velocity field was found by measurement to be brought about by the successive arrival of 'columnar disturbance modes', discussed in part 1. Agreement with the theoretical predictions is excellent. A similarity profile of the steady-state horizontal velocity is obtained, and the Froude number based on the thickness of the flowing zone is found to approach a constant value in the essentially inviscid region. The results are compared with field data from the Tennessee Valley Authority (TVA) reservoirs.

1. Introduction

In part 1 (Pao & Kao 1974), a theory was presented which identifies the successive arrival and nonlinear interactions of columnar disturbance modes as the mechanism for the development and establishment of the withdrawal layer in the selective withdrawal of a stratified fluid from a line sink in a channel of finite depth $2d$. The mean density $\bar{\rho}(Z)$ varies linearly with height. In this paper, careful experiments to verify quantitatively the theoretical findings, and to complete the full understanding of the dynamics of establishment of the flow are reported. As mentioned in part 1, the governing parameter of the problem is the Froude number F, defined as Q/Nd^2, where $2Q$ is the discharge per unit width, and the Väisälä frequency

$$N = \left(-\frac{g}{\rho_0}\frac{d\bar{\rho}}{dZ}\right)^{\frac{1}{2}}, \quad \rho_0 = \bar{\rho}(0), \quad z = Z/d.$$

The experiments were performed in a Plexiglas channel 30·5 ft long, 2 ft high and 14 in. wide, filled with a linearly stratified salt solution to a depth of 18 in. The line sink was located at mid-depth. The fluid was initially at rest, and

the discharge was started suddenly. The flow field at any subsequent time was perfectly symmetric about the mid-depth centre-line. Thus, the half-depth of the fluid was taken as d. Velocity measurements were obtained by neutrally buoyant liquid droplets, and density measurements were made by a salinity probe. Flow visualization was also obtained by vertical dye lines.

The results show clearly the following sequence of events after the initiation of the discharge: instantaneous establishment of potential flow in the whole flow field, arrival of jet-like columnar disturbance at upstream stations, development and intensification of the withdrawal layer, establishment of steady-state velocity profile with fully stagnant fluid outside the withdrawal layer. Quantitative measurements are obtained at each stage of the development and show excellent agreement with the theoretical findings of part 1.

In the steady state, a similarity profile of the horizontal velocity is obtained, and the Froude number based on the thickness of the flowing zone is found to approach a constant value in the essentially inviscid region. The results are compared with the steady-state results of part 1, with the steady-state theories of Kao (1965, 1970), Koh (1966) and Imberger (1972), as well as with the experiment of Debler (1959). Applications of the results to selective withdrawal from density-stratified reservoirs are also indicated.

2. Experimental set-up and procedure

2.1. *Experimental set-up*

The main experimental apparatus was a long channel of clear acrylic sheet, 14 in. wide, 24 in. deep and 30·5 ft long. It is shown schematically in figure 1.

A discharge box was designed so that a suddenly opened line sink could be achieved. Figure 2 is a detailed diagram. This box, which was open at the top and made of acrylic sheet, had exactly the same width as the channel. Its bottom and three sides were sealed permanently, and the remaining wall facing the long channel had a sharp-edged slot opening, positioned at a height corresponding to 9 in. from the channel bottom. The lower plate of the slot opening was fixed and sealed, while the upper part was fastened by four screws, so that the gap of the opening (and hence the discharge) could be regulated. A piece of rubber sheet glued to one side of a Plexiglas strip was used as a stopper. When it was positioned and pushed by two springs against the slot opening inside the box, the slot (i.e. the line sink) was closed. When a pump with a capacity much greater than the slot discharge withdrew water from the box, the pressure difference on the stopper increased, and immediately pushed it back, as soon as the supporting springs were removed. Thus an instantaneous opening of the line sink was achieved. During the experiment, supporting springs were removed when the water level inside the discharge box dropped below the slot opening; and a free jetting of water through the slot was guaranteed and maintained by the large capacity pump. Furthermore, no disturbances were introduced into the flow field, since they were confined inside the box.

A conductivity probe (see figure 3) was used to measure the salt content (i.e. the density of the channel fluid). Calibrations were made repeatedly at two

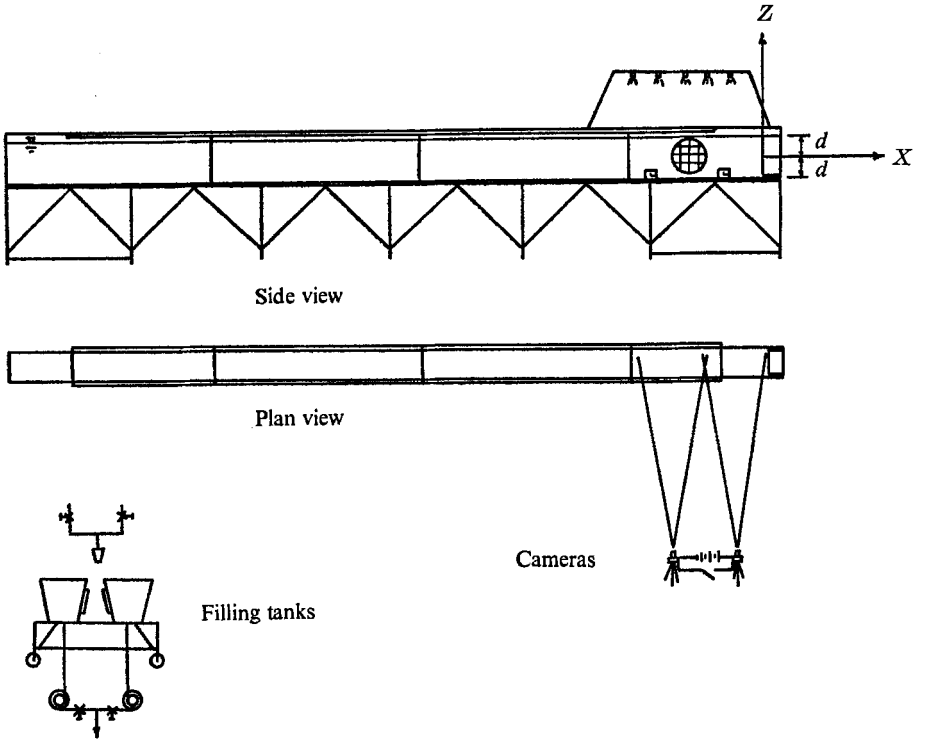

FIGURE 1. Schematic diagram of experimental apparatus.

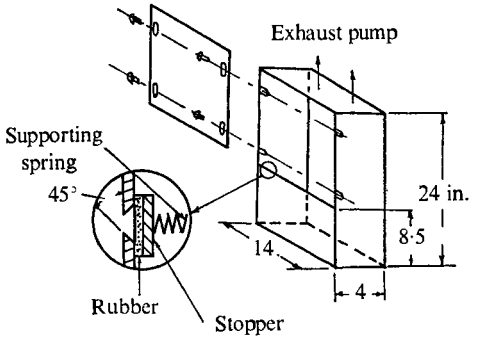

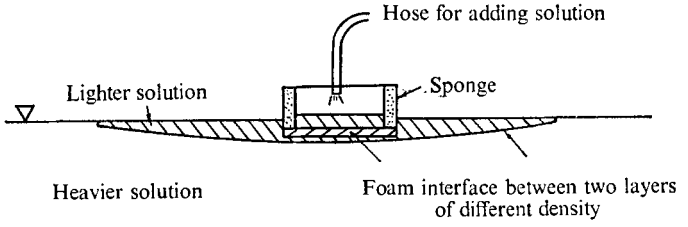

FIGURE 2. Discharge box and floater.

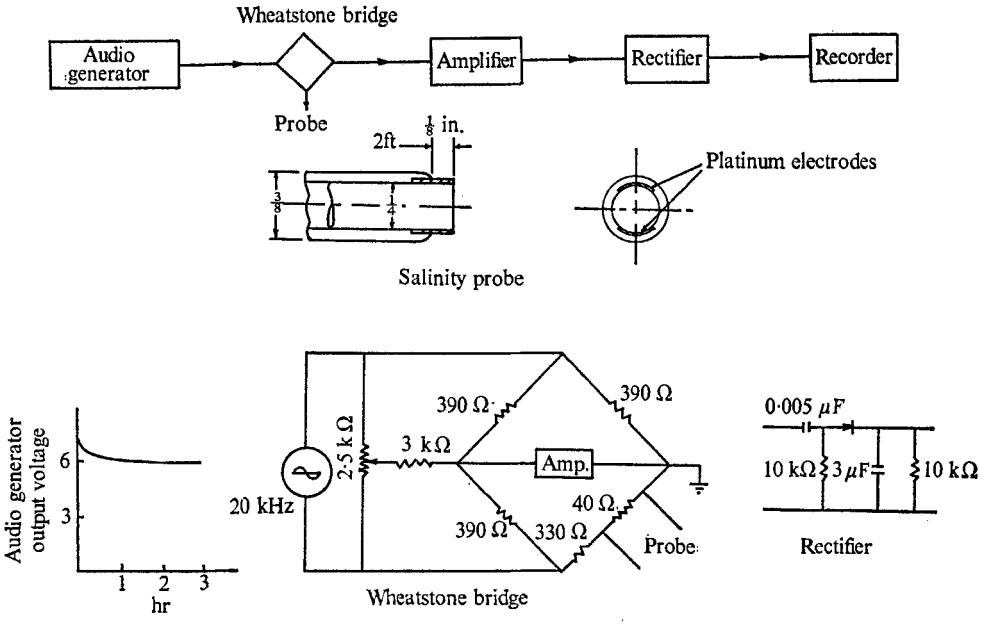

FIGURE 3. Salinity probe and circuit diagram.

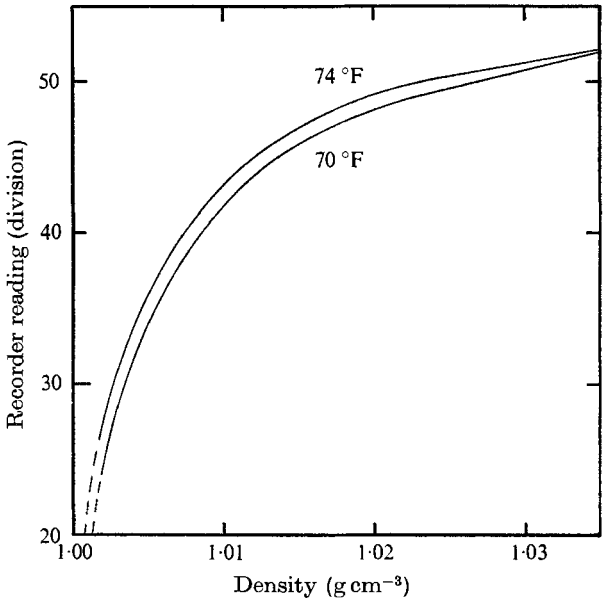

FIGURE 4. Salinity probe calibration curves.

different temperatures (70 °F and 74 °F) for the density range between about 1 g cm^{-3} to 1·035 g cm^{-3}. The calibration curve is shown in figure 4.

Two Nikon cameras with 135 mm telephoto lenses recorded the development of the flow field. They were synchronized, controlled by a single on–off push-button switch, and could be operated automatically at a maximum of 4 frames s^{-1}

or manually, frame by frame, at any desired time interval. The necessary illumination was provided by five 500 W movie lights hung directly above the channel. This arrangement of lights not only furnished a uniform illumination over a length of 8 ft, but also eliminated reflexions from the channel walls. Scales drawn on white cardboard were placed along the back wall of the channel, and two synchronized clocks with an accuracy up to 1/100 of a second, one for each camera, were so positioned in front of the channel wall that they appeared on the corner of a negative. The clock and the scale provided the basic time and spatial co-ordinates. Both nigrosine particles and oil droplets were employed as tracers of the flow field. Nigrosine crystals, on being dropped into the channel, traced out sharp black vertical streaks, through which the location of the sink centre-line (i.e. where the maximum deformation took place), and the symmetry of the flow, could easily be observed. Red droplets, diameter varying from $\frac{1}{32}$ to $\frac{1}{4}$ in., were used as the main tracer. They were a mixture of light lubrication oil, carbon tetrachloride and red dye. By choosing different ratios of oil and carbon tetrachloride, different density mixtures were obtained. Droplets in which the proportions of the ingredients differed found equilibrium at different heights in the stratified medium. But it was noticed that all droplets tended to rise extremely slowly ($< 2\,\text{in.}\,\text{h}^{-1}$), with the smaller droplets rising somewhat faster than the larger. This enabled the droplets to re-arrange themselves from a layered structure to an almost uniform distribution throughout the channel depth. The explanation of this phenomenon is as follows. Each droplet was slowly and continuously losing carbon tetrachloride, which has a specific density of 1·585, to the surrounding fluid through its spherical surface and the loss rate was thus proportional to the square of its diameter, while the volume of a droplet is proportional to the cube of its diameter. A short calculation showed that for two droplets originally of the same density but of different sizes, the density of the smaller one decreased a little more than that of the larger one. Consequently, it rose a little faster than the larger one.

2.2. *Experimental procedure*

The channel was filled with 18 distinct layers of salt water, each with a different density, to a total of 18 in. (somewhat as in Debler 1959). The equipment used for this process included a floater (figure 2), so designed that it always floated freely on the surface during the filling process. Approximately 3 h were needed to complete the filling process. The experiment was performed the day after the channel was filled. An elapsed time of about 20 h permitted the diffusion process to smooth out the abrupt density differences between adjacent layers, and therefore prompted the establishment of the desired linear density distribution.

After the overnight diffusion period, the density distribution was measured by the salinity probe and checked by a hygrometer. The results verified that a continuous linear distribution profile from the original discrete distribution is established (see figure 5). Although the measured density gradients exhibited small differences for every experiment of the same stratification, these differences would exert even less effect upon the Väisälä frequency calculation, which is proportional to the square root of the density gradient. Therefore, the average

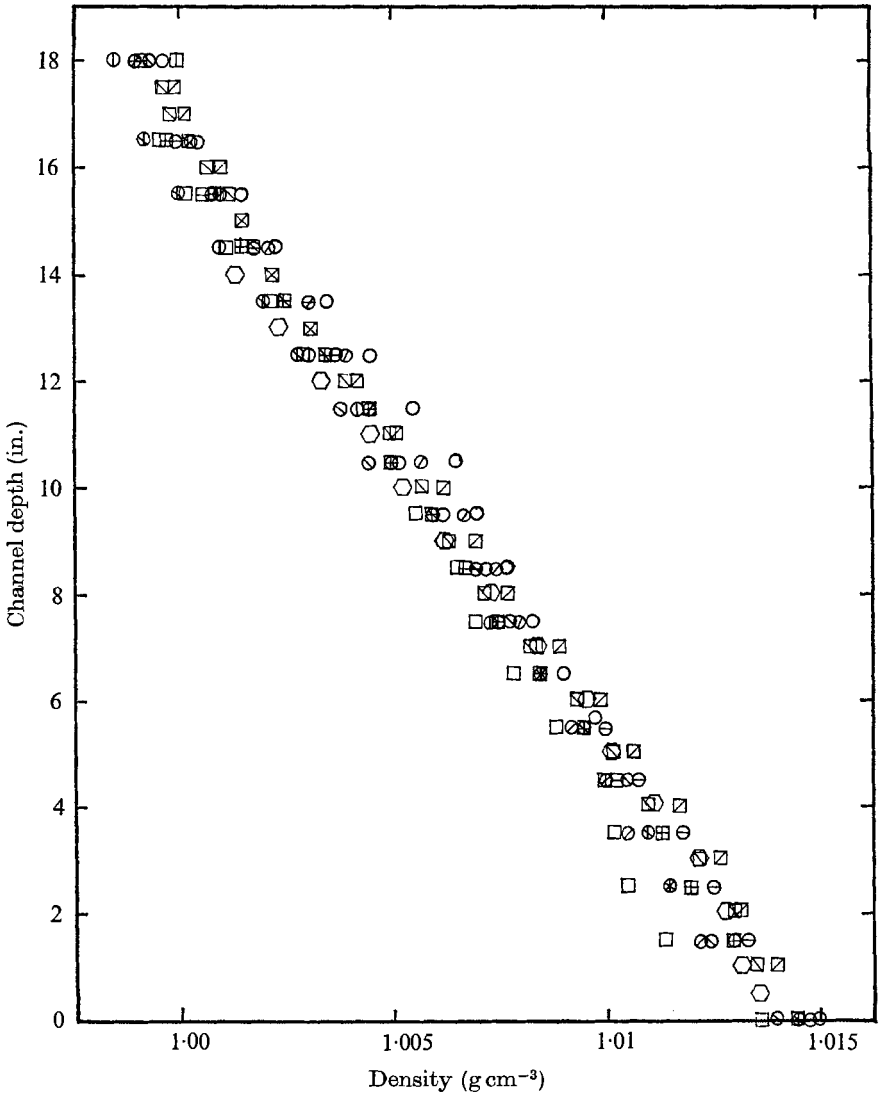

FIGURE 5. Measured density profile for sink experiments. ⊠, ⊠, ○, hydrometer measurements.

Run	*s*–1	2	0–10	11	12	*s*–3	4	7	7	4	5
	○	⊖	⊕	⊘	⊘	□	⊟	⊞	⊠	⊠	⬭

value was chosen among many measurements obtained for experiments with the same density difference between the top and bottom layers. To avoid the nonlinear density distribution near the bottom and free surface, and to minimize the viscous boundary-layer effect near the wall, the line sink was placed at the mid-depth of the stratified fluid, where the density profile was linear. For the present experiments, two values of the total density difference between the top and bottom layers were chosen. They were approximately 0·015 g cm^{-3} and 0·03 g cm^{-3}. The corresponding measured density gradients were 0·01032 g (cm^3 ft)$^{-1}$

and $0{\cdot}02093\,\mathrm{g\,(cm^3\,ft)^{-1}}$. The Väisälä frequencies based on these two values were $0{\cdot}578\,\mathrm{s^{-1}}$ and $0{\cdot}819\,\mathrm{s^{-1}}$, respectively, and were employed as time scales for normalizations.

After the linear density profile had been verified, different density droplets were introduced into the channel half an hour prior to performing the experiment. Several seconds before the line sink was opened, nigrosine particles were dropped into the channel. At the moment the sink discharge was activated, the clocks were activated.

The two cameras, which provided a combined coverage of more than 5 ft in front of the line sink, were focused on those droplets near the spanwise centre-plane of the channel. Immediately after the line sink was opened, pictures were taken at an appropriate rate.

Developed negatives were mounted and projected horizontally on a 45° oriented mirror, which reflected the projection onto a table and enabled one to analyse the flow field easily. First, scales were reproduced on a piece of white paper by the negative image. This scale was used as the basic spatial co-ordinate for each succeeding negative to match. Then the centre-line of the flow field was drawn by connecting points of maximum deformation of nigrosine streaks. Oil droplets shown on one slide at a desired position were pin-pointed and marked on the basic co-ordinates; and these same droplets on the next slide were identified and also marked. The displacement was thus easily obtained by measuring the distance between the two marks. The time interval during which the displacement took place was accurately obtained by reading the difference from the clock shown on the negatives. On dividing the displacement by the time interval, the velocity was obtained. Since the clock and the sink were activated simultaneously, the development of the flow field at a particular position could be obtained by tracing those droplets passing through that particular position at different times. The growth of the centre-line velocity u_m^* and steady-state horizontal velocity profile were obtained for several fixed distances away from the sink. That the flow was symmetrical was verified quantitatively by the results obtained from tracing oil droplets, and visually by the nigrosine dye lines. Therefore, in presenting the experimental results, no distinction is made between data obtained from droplets above the centre-line and those obtained from those below it. The discharge Q used in the calculation of F was obtained by measuring the uniform initial upstream flow (as discussed in § 3.1 below).

The sources of error that arose in the experimental and data reduction procedures described were the following. (i) *Displacement measurements from the projected slides.* The errors were negligible for the measurement of displacement down to 0·1 in. (ii) *Geometric error.* Not all the droplets were located on the spanwise centre-plane of the channel. In fact, they occupied a region 1 in. from the centre-plane. Such deviations would not show up on the photographic negatives; thus parallax corrections could not be applied to allow for them. However, since the cameras were positioned 150 in. away, a 1 in. deviation would contribute an error of 1/1·5 %, at most. (iii) *Time interval.* There was no error involved in the measurement of time interval down to $\frac{1}{100}$ of a second.

Run no.	$Re = Ud/\nu$	$F = U/Nd$	N (s^{-1})	U (in.$^{-1}$)	Temp. (°F)
s–1	3380	0·106	0·578	0·556	70
s–2	730	0·0773	0·579	0·120	77
s–3	2255	0·07125	0·578	0·371	73
s–4	2110	0·0620	0·609	0·347	73
s–5	1900	0·0558	0·609	0·312	73
s–6	827	0·0463	0·326	0·136	76
s–7	1014	0·0320	0·578	0·167	72
s–8	738	0·0292	0·462	0·1212	75
s–9	627	0·0143	0·819	0·1030	70

TABLE 1. Summary of sink experimental data. The Schmidt number $Sc = \nu/D$ is 833 in all experiments

3. Experimental results and discussions

There were nine runs, as shown in table 1. The runs with Froude numbers $F = 0{\cdot}106$, 0·07125, 0·062, 0·032 and 0·0143 were analysed in detail, and the results are presented in this section. Other runs for similar F's were used to spot check these results, to ensure repeatability of the experiments. The calculation of F is prescribed in §3.1 below. The physical sequence of events that took place after the initiation of the discharge through the line sink was observed as follows: instantaneous establishment of potential flow in the whole flow field with uniform velocity upstream from the sink before the arrival of any disturbances; development of withdrawal layer due to the arrival of disturbance modes; establishment of steady-state velocity profiles. The results are now presented and discussed in detail, following this sequence.

3.1. *Initial upstream velocity*

Initial upstream velocities U were measured at $X = -30$ in., where X is the horizontal distance from the sink. The results for four different Froude numbers are shown in figure 6(*a*). It is seen that in all cases the velocities do not vary with depth, and represent the uniform initial upstream flow as demanded by theoretical considerations. Thus, in all calculations of F, Q is equal to Ud or F is U/Nd. Initial upstream velocities were also measured for various values of X along the channel. A typical plot of the variation of the uniform velocity with X is shown in figure 6(*b*). It is seen that the variation is linear. This linear variation of the upstream uniform velocity with distance was a necessary consequence of the decrease of the free-surface level as fluid was withdrawn from the channel, as could be readily shown by a simple calculation assuming a horizontal free surface. Since the region of interest in the sink experiments was about 30 in., while the working length of the channel was 30 ft, this variation in initial upstream velocity was less than 10% there. This factor was fully taken into account in determining the initial uniform velocities for the various locations where data were deduced. A second effect of the drop in free-surface level was a reduction of the uniform velocity far upstream as time increased. However, this effect was much less

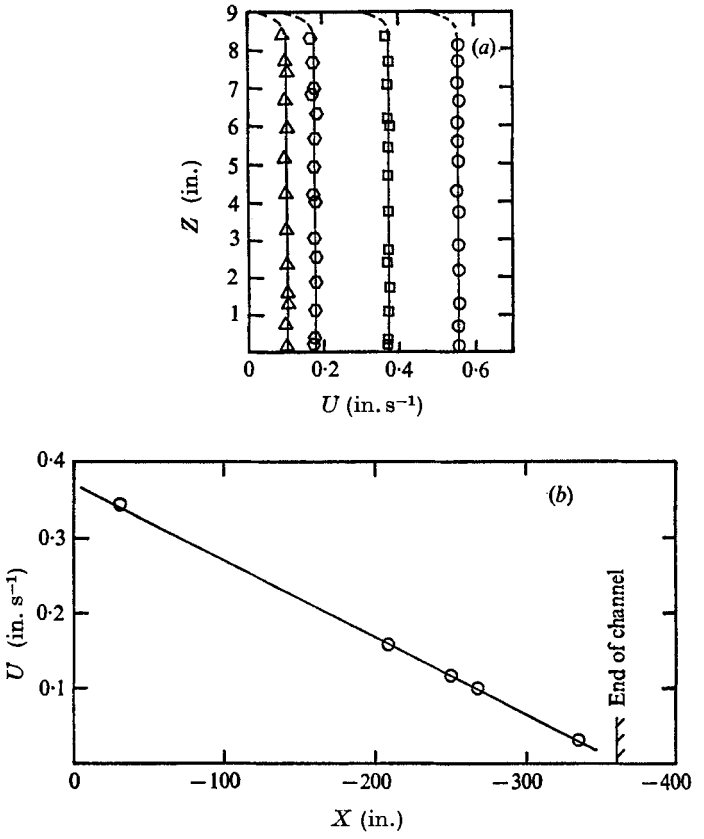

FIGURE 6. (*a*) Uniform initial upstream flow for various F measured at $X = -30$ in. △, $F = 0{\cdot}0143$; ○, 0·032; □, 0·07125; ○, 0·106. (*b*) Variation of the uniform velocity with X. $F = 0{\cdot}062$.

than 2% in all the runs, even for the total duration of the run. Indeed, for a drop of Δh in the level of the free surface the uniform velocity U' far upstream is given by

$$U' = \left[\frac{2d}{2d-\Delta h}\left(\frac{d-\Delta h}{d}\right)^{\frac{1}{2}}\right] U,$$

if we consider the discharge at a fixed upstream section to be proportional to the square root of the depth d. Thus a drop of 3 in. causes a decrease of 1·9% in the uniform velocity from its original value. For all the sink experiments, the free surface never dropped more than 3 in. at the completion of each run. Thus this second effect of the drop in the free-surface level was considered negligible.

3.2. *Development of the withdrawal layer*

Following the start of the sink discharge, the horizontal velocity u^* increased at the level of the sink, and a concentrated withdrawal layer was initiated (as shown in figures 7 and 8). The increase was substantial at $x = -0{\cdot}4$ and $t = 3$ (where $x = X/d$ and t is the dimensionless time normalized by N^{-1}) and less so

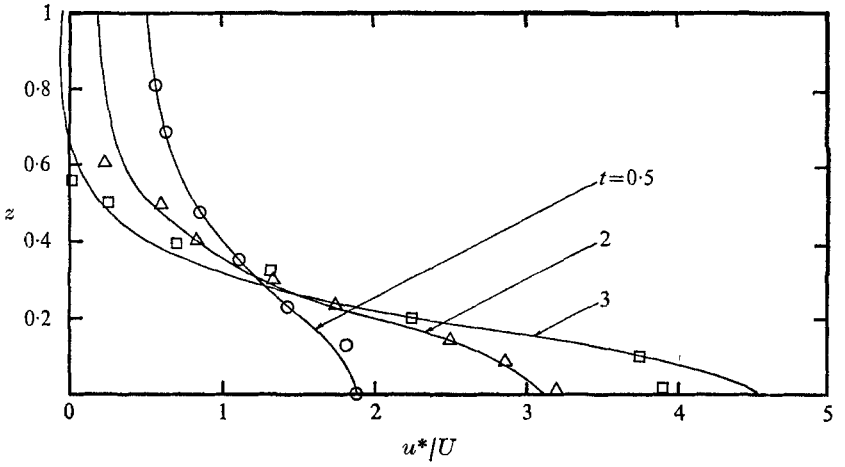

FIGURE 7. Horizontal velocity profile at $x = -0{\cdot}4$, for various t. ——, analytic theory. Experiment, for $F = 0{\cdot}0143$: △, $t = 2{\cdot}04$; □, 3·15. Experiment, for $F = 0{\cdot}062$: ○, $t = 0{\cdot}5$.

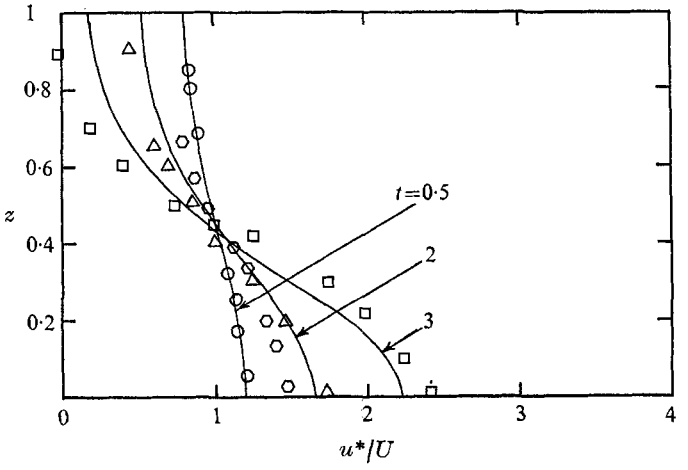

FIGURE 8. Horizontal velocity profile at $x = -0{\cdot}8$, for various t. ——, analytic theory. Experiment, for $F = 0{\cdot}0143$: △, $t = 2{\cdot}04$; □, 3·15. Experiment, for $F = 0{\cdot}062$: ○ $t = 0{\cdot}5$; ○, 1·83.

at $x = -0{\cdot}8$, whereas at that instant the velocity profile upstream at $x = -2$ remained uniform. Figures 7 and 8 also show good agreement between the experimental result and the linearized theory for this Froude number $F = 0{\cdot}0143$. From theoretical considerations in part 1, the development of the withdrawal layer is attributed to the arrival of 'columnar disturbances', which are internal gravity waves of zero frequency but finite propagation velocity, $Nd/n\pi$, $n = 1, 2, \ldots$. Part 1 showed that a line sink excited an infinite number of such modes. But, because of the non-zero uniform velocity (non-zero F) upstream, only a finite number of such modes could propagate far upstream. The most distinguished mode was the lowest ($n = 1$) and fastest-propagating mode, with propagation (or group) velocity Nd/π. Experiments for the whole range of

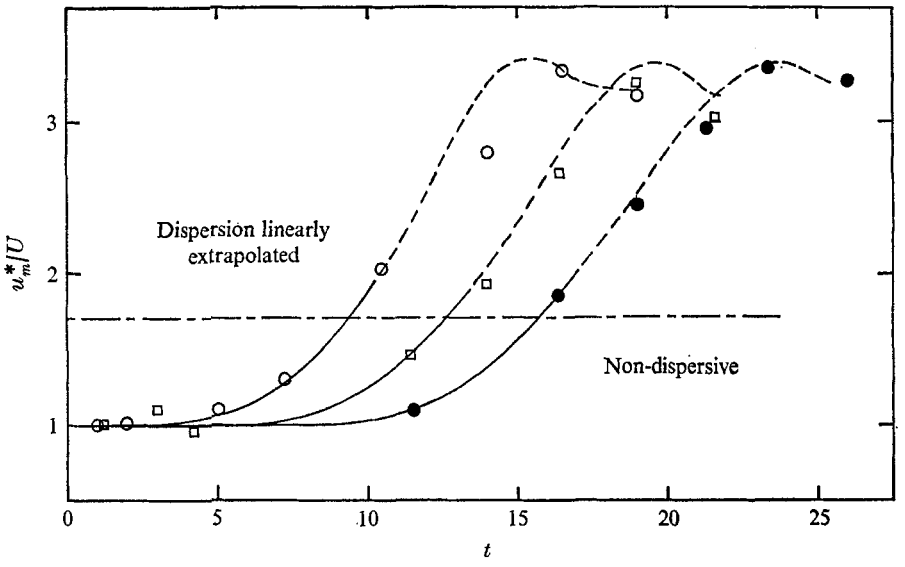

FIGURE 9. Growth of centre-line velocity with time. ——, analytic theory; – – – –, analytic theory linearly extrapolated in time. Experiment, for $F = 0{\cdot}0143$: ○, $x = -3$; □, -4; ●, -5.

Froude numbers tested indicated that, before the arrival of the lowest mode disturbance, the fluid field moved uniformly toward the sink; thus the dye streaks in that region retained their original shapes. However, those streaks started to deform successively as the lowest mode propagated upstream and encountered them. This deformation was clearly observed. So, by obtaining the arrival time and the distance in front of the line sink, the propagation speed of the lowest mode could be estimated. For $N = 0{\cdot}577\,\mathrm{s}^{-1}$ and $0{\cdot}819\,\mathrm{s}^{-1}$, $d = 9\,\mathrm{in.}$, they were found to be $1{\cdot}7\,\mathrm{in.\,s}^{-1}$ and $2{\cdot}4\,\mathrm{in.\,s}^{-1}$, respectively, which agrees very well with the predicted speeds. This agreement extends to all Froude numbers tested. Quantitative measurements of the propagation of the modes are shown in figure 9, in which the centre-line horizontal velocity is plotted against time, for various distances from the sink. The experimental points agree very well with the predictions of the theoretical result. The time needed for the disturbance to reach 1·8 times the initial uniform velocity agrees exactly with the time needed for the 'wave front' of the lowest mode to arrive, travelling at a speed equal to the wave speed minus the uniform velocity. The parts of the theoretical result for speeds greater than 1·8 are represented by dashed lines, since they are linearly extrapolated in time from calculations made at smaller times.

Typical velocity profiles at various positions and intermediate times are shown in figure 10, for a higher Froude number $F = 0{\cdot}062$. For larger Froude numbers the arrival of the lowest mode was still exactly predicted by the theoretical result as mentioned earlier since the tongue of the first mode satisfies the nonlinear equations of motion as shown in part 1. But the later development of the velocity profile involves nonlinear interaction of the modes and can no longer be predicted by the linearized theory. The experimental results in figure 10 are

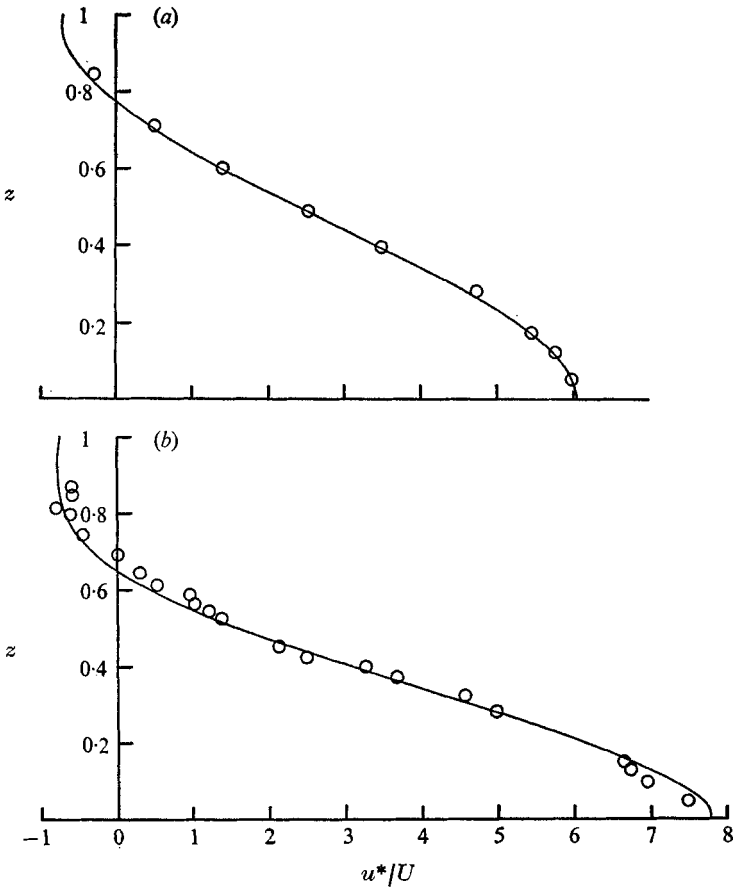

FIGURE 10. Comparison of horizontal velocity profile at intermediate times. ——, numerical solution; ○, experiment. (*a*) $F = 0{\cdot}062$, $t = 16{\cdot}1$, $x = -3$. (*b*) $F = 0{\cdot}062$, $t = 11{\cdot}3$, $x = -1{\cdot}2$.

now compared with the numerical solution of the full nonlinear Navier–Stokes equations of part 1. The agreement between the experimental points and the numerical solution is exceedingly good.

Experimental results were analysed for longer times, to examine the passage towards steady state. For that purpose, the centre-line velocity was analysed as a function of time, for various x and various Froude numbers (figures 11–14). Figure 11 shows the result for $F = 0{\cdot}0143$; the lines are from the numerical solution. For this low Froude number, one can see clearly the successive arrival and peaking of each mode. At $x = -3$, for example, one recognizes five modes in the form of five relative maxima. The higher modes do not reach their full strength, owing partly to viscous attenuation, and partly to nonlinear interaction. For example, with the kinematic viscosity $\nu = 10^{-5}\,\mathrm{ft^2\,s^{-1}}$, $1/N = 1{\cdot}75\,\mathrm{s}$, the amplitude of the fifth mode is decreased by a factor $\sim e^{-1}$. Still higher modes are more strongly damped, so that they contribute little to the further development of the velocity field. The agreement between the numerical and

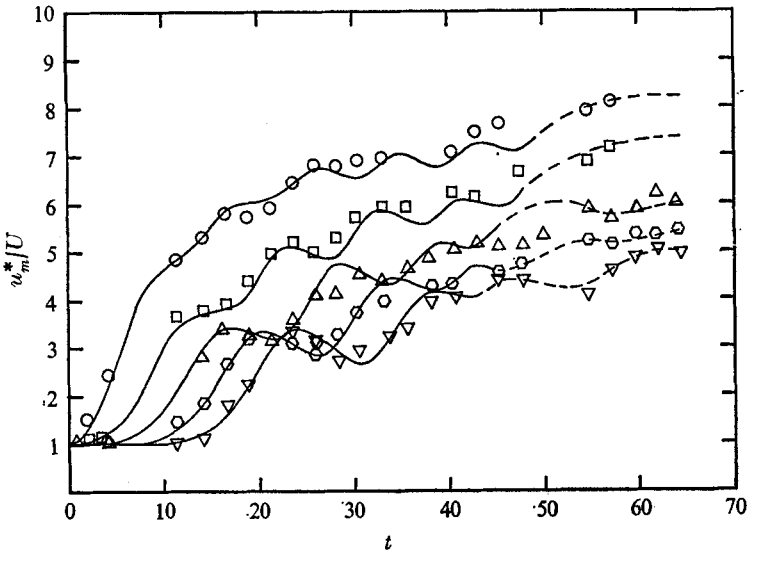

FIGURE 11. Growth of centre-line velocity with time at various x. ——, numerical solution; – – – –, connexion of experimental points. $F = 0{\cdot}0143$. ○, $x = -1$; □, -2; △, -3; ○, -4; ▽, -5.

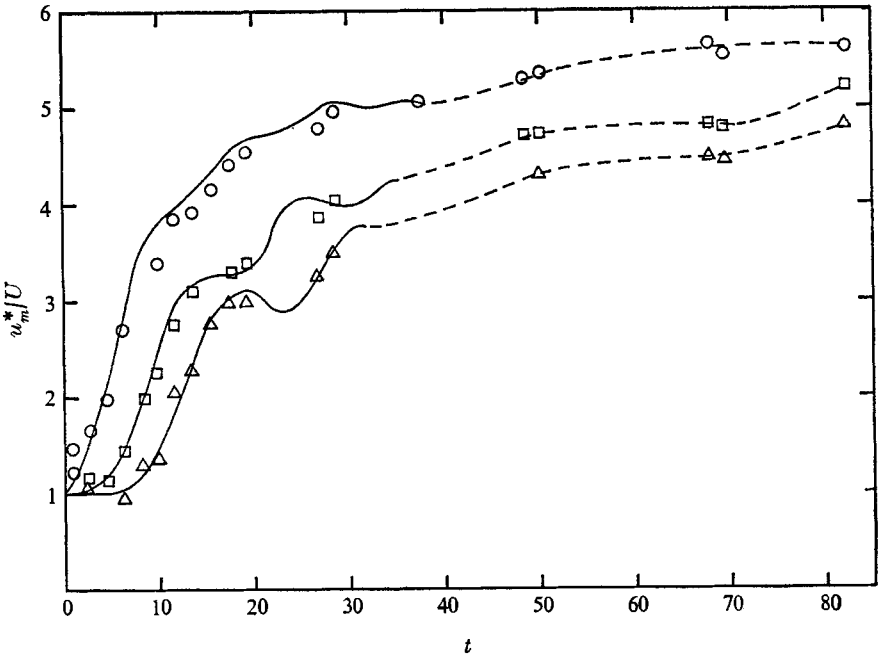

FIGURE 12. As for figure 11, except that $F = 0{\cdot}032$.

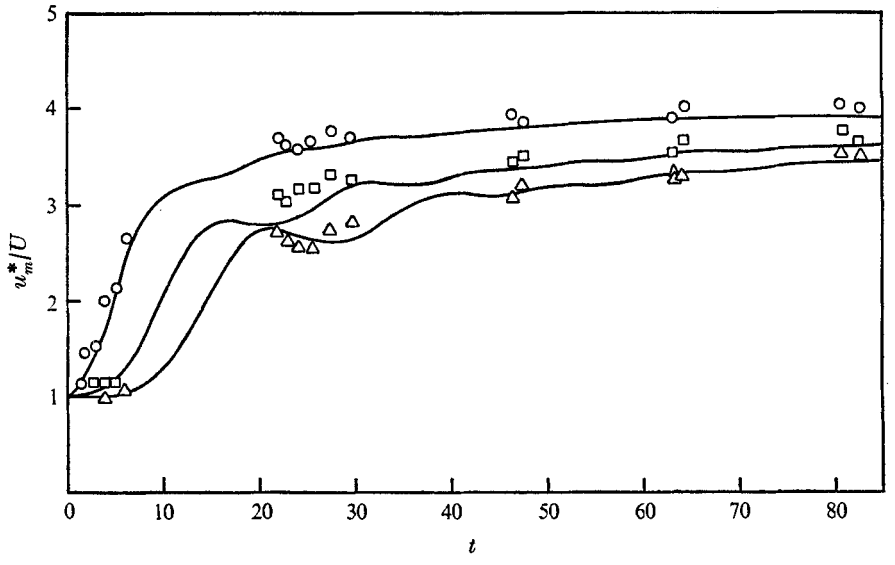

FIGURE 13. As for figure 11, except that $F = 0{\cdot}07125$.

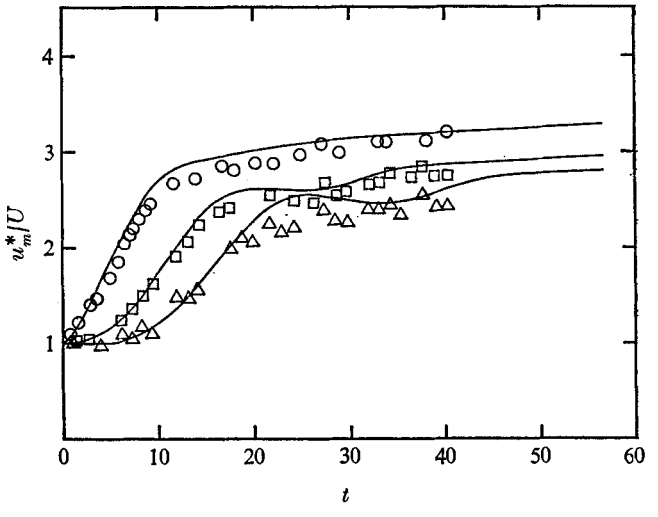

FIGURE 14. As for figure 11, except that $F = 0{\cdot}106$.

experimental results is again excellent. Portions of the plot were also shown in figure 9, where the experimental results were favourably compared with the linearized theory. In this case, one may conclude overall agreement between analytical, numerical and experimental results. Furthermore, the flow has essentially reached a steady state in the region from the sink to $x = -5$ at $t = 70$.

Figure 12 shows a similar result for $F = 0{\cdot}032$. Nonlinear effects now become the dominant factor, after the passage of the first mode, and steady state is reached in a shorter time. Figure 13 is for $F = 0{\cdot}07125$; and figure 14 is for $F = 0{\cdot}106$. In all cases, there is really superb agreement between numerical

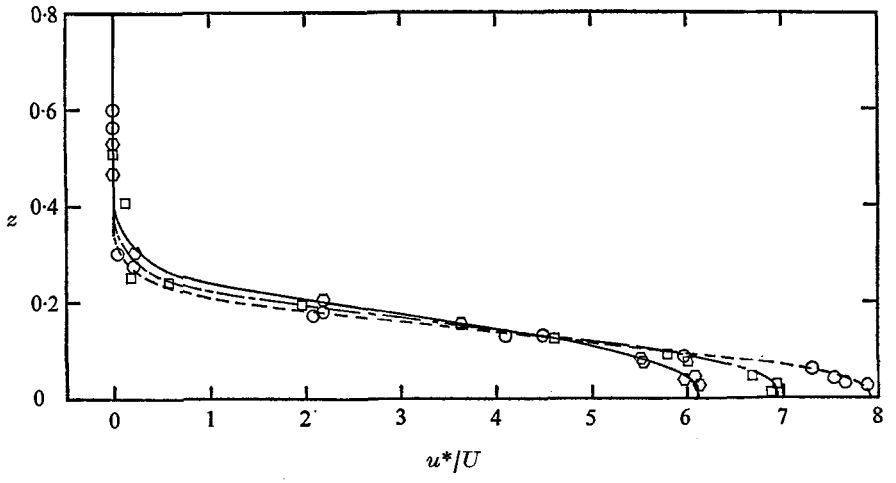

FIGURE 15. Steady-state horizontal velocity profile. $F = 0{\cdot}0143$. ○, $x = -1$; □, -2; △, -3.

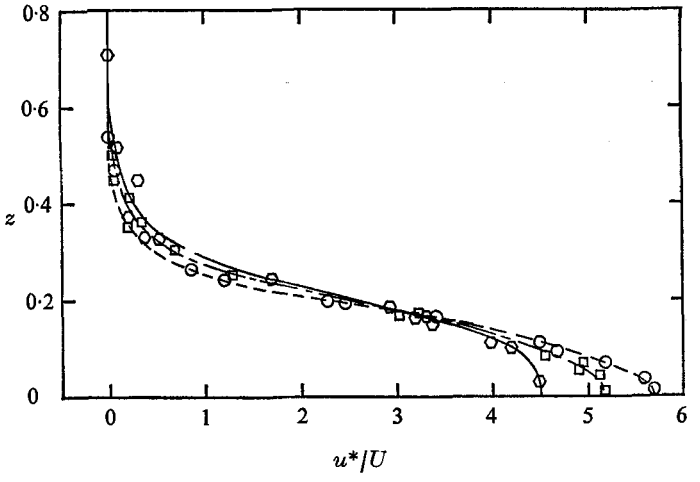

FIGURE 16. As for figure 15, except that $F = 0{\cdot}032$.

and experimental results. The steady state is reached in shorter and shorter times as the Froude numbers are increased. In figure 14, the numerical result is carried further than the experimental. For this large Froude number, only two modes of columnar disturbances can propagate upstream. The nonlinear effect is very strong here, but the first mode retains the features described by the analysis. Nonlinear effects appear to have suppressed the other mode. The viscous effect is largely absent in this case.

3.3. *Steady-state velocity profile*

In §3.2 we said that the flow at any station eventually reached a steady state. The steady-state velocity profiles at $x = -1$, -2, and -3 are shown in figures 15–17, for four different Froude numbers. In all cases, the steady-state profile

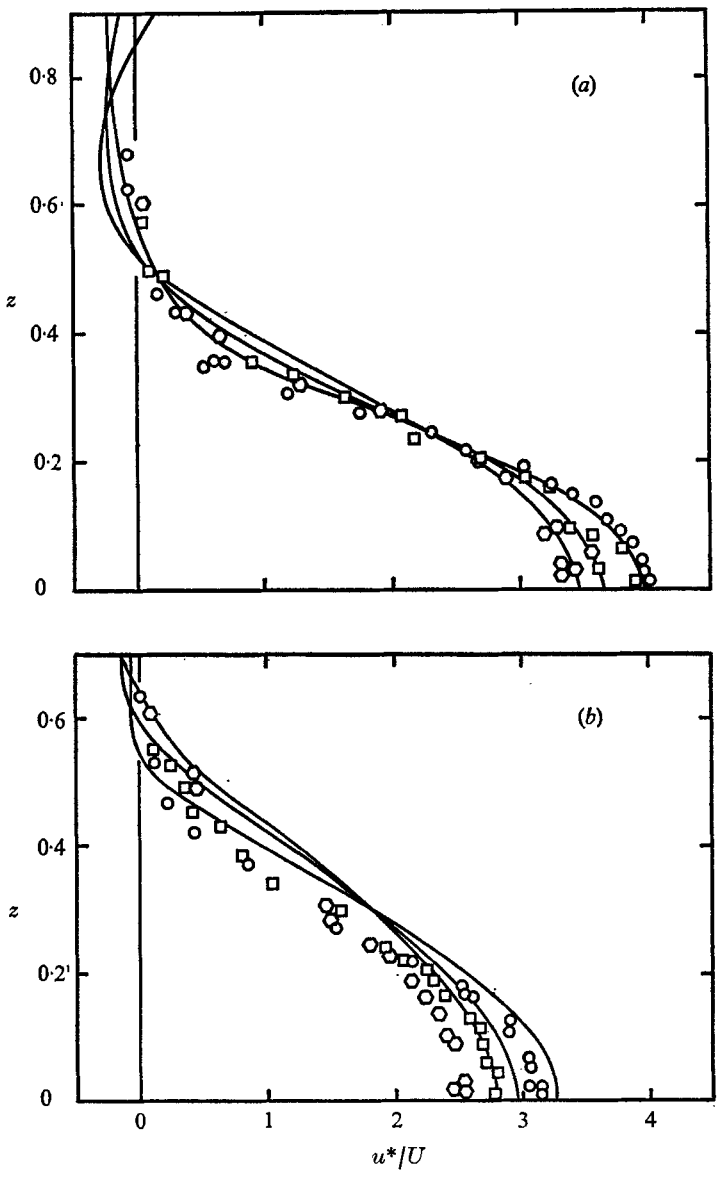

FIGURE 17. Steady-state horizontal velocity profile. ——, numerical solution; ○, $x = -1$; □, -2; △, -3. (*a*) $F = 0{\cdot}07125$. (*b*) $F = 0{\cdot}106$.

indicates markedly the existence of a completely stagnant zone and a flowing or withdrawal layer; in no case is there any indication of measurable reverse flow. The withdrawal layer becomes more and more concentrated as F decreases, which is in agreement with the interpretation that the flow field is made up of the columnar disturbances propagating upstream from the sink. In figure 17 the steady-state numerical results are shown as solid lines. The comparison is good.

An interesting result is obtained when all the data from the experiments are

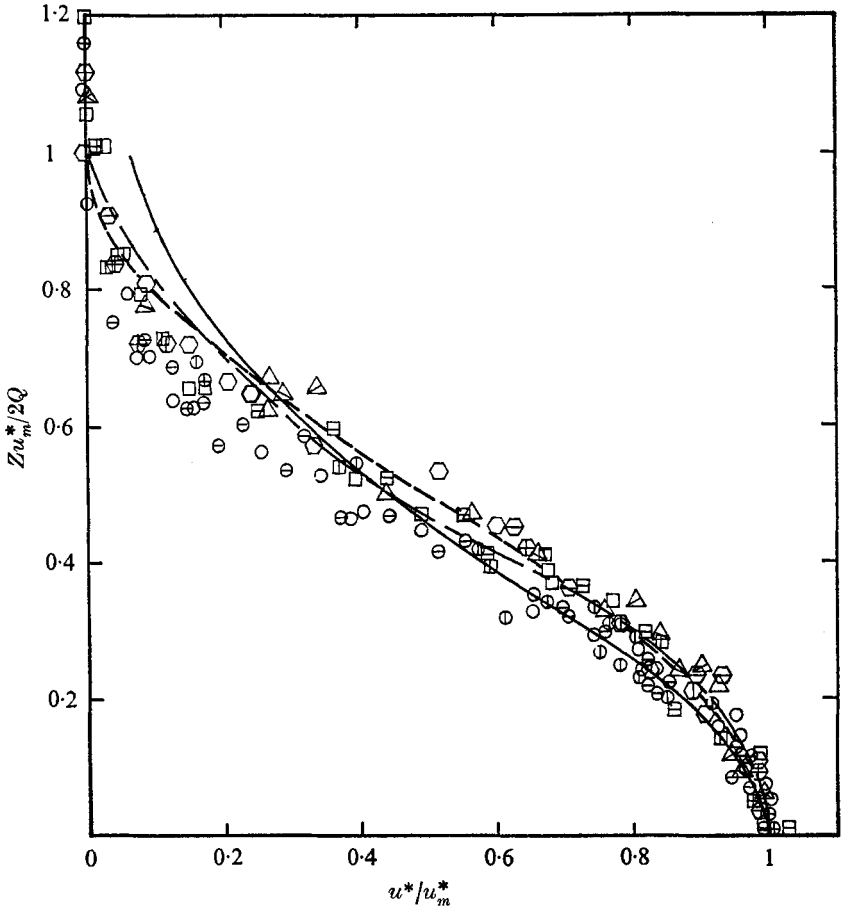

FIGURE 18. Steady-state horizontal velocity profiles at various F, compared with Imberger's result (——), Koh's (—·—) and the numerical result of part 1 (– – – –).

F	0·106			0·07125			0·032			0·0143		
x	−1	−2	−3	−1	−2	−3	−1	−2	−3	−1	−2	−3

plotted in the form u^*/u_m^* against $Zu_m^*/2Q$. This is done in figure 18, which shows that the experimental points for all the experiments with F between 0·0143 and 0·106 essentially collapse into a single curve (which means that the profiles are similar when plotted in this manner). Furthermore, the similarity velocity profile has the same shape as the forward-moving portion of Koh's (1966) solution for the linearized viscous–diffusive case, which in turn differs little from the non-linear large Reynolds number integral solution of Imberger (1972).

This result for the steady state was found from the numerical results given for $0{\cdot}032 < F < 0{\cdot}20$ in part 1, where it was shown that the profiles are very well represented by the single expression

$$\frac{u^*}{u_m^*} = \begin{cases} \frac{1}{2}(1+\cos\pi\eta) & \text{for} \quad 0 \leqslant |\eta| \leqslant 1, \\ 0 & \text{for} \quad |\eta| \geqslant 1, \end{cases}$$

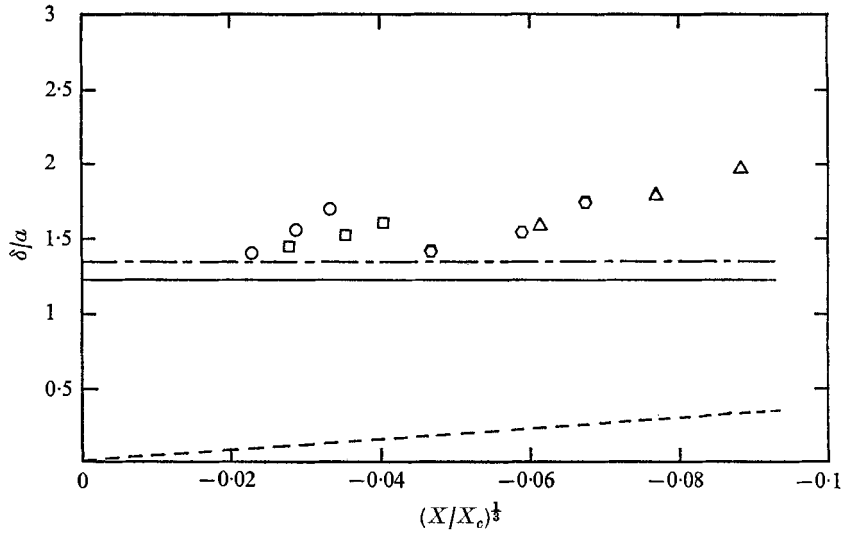

FIGURE 19. Experimental withdrawal-layer thickness, at $x = -1, -2, -3$, compared with Debler's result (—·—), Kao's (——) and Koh's (– – – –). ○, $F = 0{\cdot}106$; □, 0·07125; ○, 0·032; △, 0·0143.

$$X_c = (2F)^{\frac{1}{3}}(\nu D)^{-\frac{1}{2}} d^3 N = 3{\cdot}76 \times 10^7 F^{\frac{3}{2}} N.$$

where $\eta = Zu_m^*/2Q$. This cosine curve is marked 'numerical' in figure 18. The experimental data fit the numerical curve better than the theories of Koh and Imberger.

In the present experimental results, $Re = Ud/\nu$ ranges from 627 for $F = 0{\cdot}0143$ to 3380 for $F = 0{\cdot}106$; Imberger's experimental results are for lower Re and F, with Re ranging from 0·5 to 20; and Koh's results are in the creeping-flow regime, with very low Re and F. Furthermore, in view of the numerical results of part 1, this similarity profile does not change given any $F < \pi^{-1}$ and the full range of Re, extending to the inviscid limit. That this similarity extends over such a great range is perhaps not surprising, since the dynamics of establishment are essentially governed by the arrival of the lower columnar disturbance modes and their interaction. The profile obtained by plotting $Zu_m^*/2Q$ against u^*/u_m^* is not a sensitive check on any theoretical result. A more rigorous test of theoretical prediction is, of course, to compare u_m^* along the centre-line (as in figures 11–14). Once the value u_m^* is verified, the check on the profile shape also follows (as in figures 8 and 10).

In the steady state, the thickness of the flowing zone at various distances upstream is of great importance. From a steady inviscid free-streamline theory, Kao (1965, 1970) arrived at the result that the withdrawal half-thickness δ is given by $\delta/a = (2F_1)^{-\frac{1}{2}}$, where $a = (2Q/N)^{\frac{1}{2}}$ and $F_1 = 0{\cdot}33$ (F_1 is the Froude number based on the withdrawal thickness, i.e. $F_1 = Q/N\delta^2$), or $\delta = 1{\cdot}23a$, which is in agreement with Debler's (1959) experimental result; the latter indicated that $\delta = 1{\cdot}34a$. Koh (1966) found that, in the viscosity-dominated regime of creeping flow, the withdrawal thickness increases in value from zero according to $(X/X_c)^{\frac{1}{3}}$, where $X_c = (2F)^{\frac{3}{2}}(\nu D)^{-\frac{1}{2}} Nd^3$ is a viscous–diffusive scaling length, and D is the

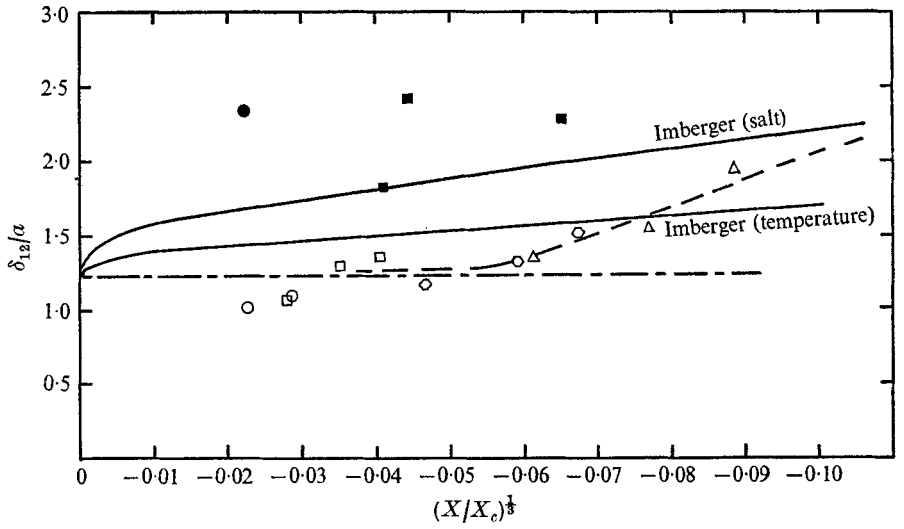

FIGURE 20. Experimental results, at $x = -1, -2, -3$, compared with field data from TVA Water Resources Research Reports. ——, Imberger's result; —·—, Kao; ●, Fontana; ■, Cherokee; ○, $F = 0{\cdot}106$; □, 0·07125; ○, 0·032; △, 0·143.

$$X_c = (2F)^{\frac{3}{2}}(\nu D)^{-\frac{1}{2}} d^3 N = 3{\cdot}76 \times 10^7 F^{\frac{3}{2}} N.$$

diffusivity. It is of interest to plot δ/a against $(X/X_c)^{\frac{1}{3}}$ for the present experimental results (as in figure 19). In this plot δ is given by $2Q/u_m^*$, so that δ is close to the width where the velocity first becomes zero (see figure 18). The present result compares reasonably well with Kao's (1970) steady-state theory, and the qualitative experimental result of Debler. The value of F_1 based on δ approaches a constant value of $0{\cdot}20 \pm 0{\cdot}02$ in the essentially inviscid region (near-field variation of δ for $X/X_c < 0{\cdot}05$ is, of course, excluded). Koh's theoretical result is also indicated on the plot. The present experimental results are further compared with Imberger's theoretical prediction in figure 20. For that purpose, the withdrawal thickness δ_{12} is defined to be the width at which the velocity has dropped to $\frac{1}{12}u_m$, the definition adopted by Imberger (1972). Imberger's result essentially adds a viscous layer growing in thickness in proportion to $(X/X_c)^{\frac{1}{3}}$ on to the inviscid core given by Kao (1970). The present experiments, conducted at high Re, indicate that viscous action is present for $(X/X_c)^{\frac{1}{3}} > 0{\cdot}05$, and that the data do tend towards Imberger's theory as $(X/X_c)^{\frac{1}{3}}$ increases; but the data points all fall below Imberger's curve. The same trend was observed by Imberger (1972). Agreement between the experimental data and the numerical solution of figure 16 of part 1 is good. The value of F_1 is now $0{\cdot}30 \pm 0{\cdot}02$ in the inviscid region, owing to a change in the definition of withdrawal thickness.

It was pointed out in part 1 that, for X_c large and X/X_c very small, say $(X/X_c)^{\frac{1}{3}} < 0{\cdot}05$, the effect of viscosity is no longer important, and X_c is no longer an appropriate scaling length. For that regime, it is more appropriate to plot δ/a against $x^{\frac{1}{3}}$. The present experimental data for $F = 0{\cdot}106$ are now inserted into this plot (figure 21). Agreement between the numerical and experimental values for $F = 0{\cdot}106$ is very good.

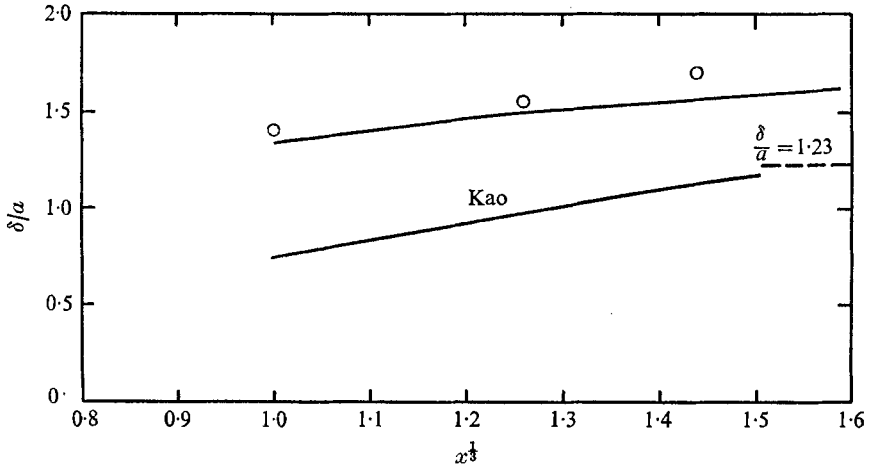

FIGURE 21. Numerical withdrawal-layer thickness, as a function of $x^{\frac{1}{3}}$, for $F = 0{\cdot}106$.

Hence, the steady-state complete flow field is easily described when the discharge Q, Väisälä frequency N, and the viscosity and diffusion coefficients are specified. That is, for any x, δ is known from figure 19 or 21; so u_m^* is known from the definition of δ, and the velocity profile is given by

$$\frac{u^*}{u_m^*} = \begin{cases} \frac{1}{2}(1+\cos\pi\eta) & \text{for} \quad 0 \leqslant |\eta| \leqslant 1, \\ 0 & \text{for} \quad |\eta| \geqslant 1, \end{cases}$$

for all $F < \pi^{-1}$ down to $F \sim O(10^{-3})$ when reverse flow is present for $|\eta| > 1$ (as shown by Koh 1966).

4. Applications of the results to selective withdrawal from density-stratified reservoirs

To predict water quality in selective withdrawal from density-stratified reservoir, the estimate of the thickness of the withdrawal zone is of primary importance. On the basis of the inviscid theory and field data, Wunderlich & Elder (1968) proposed the formula $\delta = 2{\cdot}5a$ for field applications. Field data from the Fontana and Cherokee reservoirs of the TVA system are plotted in figure 20, again using the definition for δ_{12} proposed by Imberger. A discrepancy exists between field data and laboratory and theoretical findings. An explanation of the discrepancy is now feasible, in view of our new understanding of the dynamics of establishment. For example, owing to topographical influence, or unsteadiness, many of the modes may not have reached an upstream location, and thus may have caused a broadening of the withdrawal layer. Such ideas are presently being pursued in the Hydrodynamics Laboratory.

In the TVA reservoirs, the outflows are characterized by steady high discharges during power peaking operations, and by low to zero discharges at other times. The unsteady flows are also of great importance to water quality control. The response of the stratified fluid to the initiation of penstock intake is now clearly

Name of station	Distance from dam (miles)	Time for turbine discharge to reach max (h)	Discharge ($ft^3\ s^{-1}$)		Response time		
			Mean	Max.	t_A	t_B (h)	t_C
Mile 61·6	0·6 (15 Aug. 1966)	1	3886	6000	3	5	6
Mile 65·5	4·5 (15 Sept. 1966)	3	4242	6750	6	13	15

TABLE 2. Wunderlich & Elder (1968): t_A, time lag between turbine start-up and resumption of downstream water movement; t_B, time lag between beginning of full power house discharge and the establishment of maximum velocity at El centre-line intake; t_C, time lag between turbine start-up and the establishment of maximum velocity at El centre-line intake

Mile	t_A (h)	t_B (h)	t_C (h)
61·1	2–3	5	5–6
65·5	9	11	14

TABLE 3. Estimated response times

understood in terms of the dynamics of establishment. The field data from the Fontana reservoir are given by Wunderlich & Elder (1968); see also table 2.

The density-stratification data at Mile 61·6 gives a depth of the stratified layer of 200 ft and a Väisälä frequency of $0{\cdot}02\ s^{-1}$. If we take the average width of the reservoir to be 2000 ft, and the depth to be 350 ft, the uniform velocity would be $0{\cdot}01\ ft\ s^{-1}$, and the overall densimetric Froude number $F < 0{\cdot}005$. For this low F, the dimensionless times to establish a steady state may be estimated at 140 from the time of the first arrival of the disturbance or 2 h for $N = 0{\cdot}02\ s^{-1}$. The velocity C_1 of the lowest mode is equal to Nd/π, where d is the half-depth of the stratified layer or $C_1 = 0{\cdot}6\ ft\ s^{-1} = 0{\cdot}41\ miles\ h^{-1}$. In Wunderlich & Elder (1968, figure 28), there was an upstream flow (or forward flow) of $0{\cdot}1\ ft\ s^{-1}$ in the reservoir at Mile 61·6 when the turbine discharge was initiated. Thus the velocity with which the first columnar disturbance would arrive was 0·6–0·1 ft s^{-1} or 0·34 miles h^{-1}. So for Mile 61·6 (0·6 miles from the dam), the time needed for the arrival of the first disturbance was approximately 2–3 hr, on taking into account the 1 h start-up time for the turbine to reach maximum discharge. The values for the response times estimated from our present study are given in table 3.

Agreement between the field data and the predicted values given above is excellent for Mile 61·6, where information is complete. For Mile 65·5 we have used the same basic information as for Mile 61·6, with the exception that no forward flow was present in the field test. The actual density against depth profile at Mile 65·5 is not available in this report. Agreement between predicted and field data is still reasonable, in view of the lack of more precise field information on the stratification conditions existing in the reservoir, and in view of the much greater distance to the station.

The authors are indebted to the Atmospheric Sciences Section, National Science Foundation, for their support under grant GA-23784.

REFERENCES

DEBLER, W. R. 1959 Stratified flow into a line sink. *J. Eng. Mech. Div., Proc. A.S.C.E.*, **85**, 51–65.

IMBERGER, J. 1972 Two-dimensional sink flow of a stratified fluid contained in a duct. *J. Fluid Mech.* **53**, 329–349.

KAO, T. W. 1965 A free-streamline solution for stratified flow into a line sink. *J. Fluid Mech.* **21**, 535–543.

KAO, T. W. 1970 Free-streamline theory for inviscid stratified flow into a line sink. *Phys. Fluids*, **13**, 558–564.

KOH, R. C. Y. 1966 Viscous stratified flow towards a sink. *J. Fluid Mech.* **24**, 555–575.

PAO, H.-P. & KAO, T. W. 1974 Dynamics of establishment of selective withdrawal of a stratified fluid from a line sink. Part 1. *J. Fluid Mech.* **65**, 657.

WUNDERLICH, W. O. & ELDER, R. A. 1968 Evaluation of Fontana Reservoir field measurements. *A.S.C.E. Specialty Conf. on Current Research into Effects of Reservoirs on Water Quality*, Portland, Oregon.